Adaptive-Size Fiducial-Marker Detection with Dual-Stage Kalman Filtering for Precision UAV Landing

K. P. Ayodele[1]*, P. T. Okewunmi[1], S. O. Akinola[1], A. A. Ogunseye[1], M. I. Eghrudje[1], F. B. Offiong[2], S. P. Olayiwola[1], A. R. Lawal[3], F. O. Akinluyi[4], A. A. Ishola[5]

[1]Department of Electronic and Electrical Engineering, Obafemi Awolowo University, Ile-Ife, Nigeria
[2]Department of Electrical and Electronic Engineering, School of Computing, Engineering and Built Environment, Glasgow Caledonian University, United Kingdom.
[3]Department of Computer Science and Engineering, Obafemi Awolowo University, Ile-Ife, Nigeria.
[4]Department of Remote Sensing & Geoscience Information Systems, Federal University of Technology, Akure, Nigeria.
[5] Department of Mechatronics Engineering, Federal University of Agriculture, Abeokuta, Nigeria.

ABSTRACT: Precision UAV landing systems face significant challenges with traditional fixed-marker approaches, particularly under varying environmental conditions and integration scenarios. This paper presents a novel approach combining dynamically sized fiducial markers with dual-stage Kalman filtering to address these limitations. The methodology utilizes a 13.3-inch e-ink display showing ArUco markers that dynamically scale from 16.7 cm to 2.8 cm during descent, actively reducing marker size while accounting for e-ink display refresh constraints through predictive state estimation. A vision system processes frames at 30Hz through an optimized detection pipeline, while the dual-stage Kalman filter handles both vehicle state estimation and parameter adaptation, managing display transition dynamics. The system's universal protocol framework enables compatibility with both integrated and unknown UAV platforms through a dual-mode detection approach, combining passive visual detection with active altitude signalling. Experimental validation using a DJI F450 platform with downward-facing camera demonstrates the system achieves mean landing errors of 1.95 cm under wind conditions up to 15 km/h, representing a 59% improvement over fixed-marker approaches. The e-ink display enables reliable marker detection up to 14.2m altitude under direct sunlight conditions, outperforming LCD displays which become undetectable in bright conditions. Pixel-wise RMSE improved from 150.3 to 140.5 (x-axis) and 170.8 to 151.4 (y-axis) over four sequential landings, demonstrating robust operation across varying integration scenarios.

KEYWORDS: Precision landing, UAV, Adaptive fiducial marker, Dual-stage Kalman filter, E-ink display

[Received Nov. 13, 2024; Revised June 26, 2025; Accepted July 16, 2025] Print ISSN: 0189-9546 | Online ISSN: 2437-2110

I. INTRODUCTION

The proliferation of unmanned aerial vehicles (UAVs) across industrial applications has intensified the need for reliable autonomous operations, particularly for rotary-wing platforms capable of vertical descent and precision hovering. For these systems, accurate landing capability has emerged as a critical requirement. Traditional navigation approaches rely primarily on Global Navigation Satellite Systems (GNSS), which typically provide positioning accuracy in the meter range under optimal conditions. While sufficient for general navigation, this accuracy deteriorates significantly in urban canyons, under dense canopy, or near large structures - precisely the environments where many critical UAV operations occur. Even with Real-Time Kinematic (RTK) corrections, GNSS-based systems struggle to maintain consistent centimeter-level accuracy, particularly during the critical final approach phase of landing operations.

Vision-based landing systems have emerged as a promising solution for achieving high-precision landings. These systems offer several advantages: they operate independently of external navigation infrastructure, provide direct feedback for relative positioning, and can achieve high accuracy at close range. However, they face a fundamental challenge: the trade-off between marker size and detection reliability across varying altitudes.

This research introduces a novel solution to the marker size-detection trade-off through adaptive marker presentation. The system dynamically adjusts displayed marker size during descent, maintaining optimal detection characteristics throughout the landing sequence. Implementation requirements include high contrast ratio, outdoor visibility, low power consumption, and sufficient resolution for precise marker rendering. Among available technologies - LCD, OLED, LED matrices, and bistable displays - electronic paper (e-ink) was selected for its ultra-low power consumption,

*Corresponding author: kayodele@oauife.edu.ng
doi: http://doi.org/10.63746/njtd.v22i4.3078

excellent sunlight visibility, and cost-effectiveness, despite refresh rate limitations. The approach combines this display system with a sophisticated dual-stage Kalman filtering framework that handles both state estimation and parameter adaptation while managing display transition dynamics. While this paper demonstrates the concept using an e-ink display implementation, the approach can be adapted to various display technologies based on specific operational requirements such as update rate, power consumption, or lighting conditions.

The primary contributions of this work include: a theoretical framework for adaptive fiducial marker systems that dynamically optimize marker characteristics based on UAV state; a dual-stage Kalman filtering approach that simultaneously handles state estimation and parameter adaptation while managing e-ink display transition dynamics; a practical implementation demonstrating that a simple marker size reduction strategy achieves significant improvements in landing precision; a universal landing protocol framework enabling standardized implementation across different UAV platforms and experimental validation demonstrating sub-2 cm landing accuracy.

II. RELATED WORK.

Vision-based UAV landing has evolved from simple template matching to sophisticated marker-based approaches, driven by the limitations of GPS-based systems in achieving centimeter-level accuracy (Claro et al., 2023; Wubben et al., 2019). The introduction of fiducial markers, particularly ArUco markers, revolutionized precision landing by providing robust 6-DOF pose estimation with relatively low computational overhead (Ulrich et al., 2022).

Recent work has focused on enhancing landing accuracy through improved marker detection and pose estimation algorithms. Nguyen et al. (2017) determined how to safely and a rotor drone in the absence of GPS signals by using their remote marker-based tracking algorithm based on the visible light camera. Cabrera-Ponce et al. (2017) presented a methodology for autonomous landing based on multiscale image processing approach which helps to detect landing zones at different scales. They used a template-based matching in an image pyramid scheme in combination with edge detector.

The integration of marker-based vision with inertial measurements has emerged as a key strategy for robust landing performance. Yuan et al. (2017) proposed in their study that in the case where vision-based position estimation became unavailable, the drone will still navigate towards the defined position using IMU sensors. For this study Kalman filter and PID controller were used to achieve better performance. Wang et al. (2017) investigated autonomous landing of multi-rotor UAVs on a moving platform. From conducted experiments they obtained an average landing error of 10cm from the pad center. Borowczyk et al. (2017) used a Kalman filter to estimate the position of a Micro Aerial Vehicle (MAV) relative to the landing pad fusing together measurements from the MAV's onboard INS, a visual fiducial marker and a mobile phone. Wu et al. (2019) proposed a six-degrees-of-freedom (DOF) pose estimation solution for UAV landing based on an artificial marker and a micro-electromechanical system (MEMS) inertial measurement unit (IMU). The visual/inertial system was fused with an Extended Kalman filter and this improved the roll and pitch accuracy by about 33% and 54%.

Recent innovations in marker systems have attempted to address the fundamental trade-off between detection range and precision. While fixed markers provide reliable performance within their designed operating range, they face inherent limitations in achieving consistent accuracy across varying altitudes. Piczynski et al. (2024) described a deep learning-accelerated image processing pipeline for accurate detection and relative pose estimation of the UAV with respect to a landing pad even amidst challenging conditions.

Park et al. (2024) combine an image filter with a single-stage Kalman filter to improve the robustness of fixed-size ArUco marker detection. Their system achieved 2.7 cm landing error in simulation and 9.47 cm mean error in outdoor flight tests under light disturbances. In contrast, the proposed system adapts the rendered marker size continuously to maintain the image within 20–40 % of the camera's field of view, employs a dual-stage Kalman structure that learns the UAVs inner-loop PID latency, and demonstrates a 1.95 cm mean error across 20 real-world landings—an order-of-magnitude improvement under full-flight conditions.

The concept of adaptive landing systems represents a recent paradigm shift in precision UAV operations. The use of active displays for landing guidance has been explored in limited contexts. Arent at al. (2009) investigated the landing performance of pilots using a synthetic vision display which included perspective objection of the flight path. Yasentsev et al. (2021) considered using passive reflectors for improving UAV landing with about 1-3m position error of successfully landed drone. Basiaens et al. (2021) demonstrates the potential of received signal strength (RSS) Visible light positioning (VLP) with a single photodiode (PD). The study proposes that a PD-equipped drone self-localized with respect to Light emitting diodes (LEDs) that are integrated into the landing zone. Their system yielded a sufficient landing accuracy of below 3.5cm.

III. SYSTEM DESIGN AND PROBLEM FORMULATION

A. System Overview

Consider the problem of precisely landing a rotary wing UAV equipped with a downward-facing camera, as depicted in Figure 1. The camera has a field of view with dimensions W_F and L_F (in pixels), within which lies a fiducial marker of size $L_M \times W_M$ either printed on a flat surface or displayed on a screen. The landing objective is to minimize positioning errors e_H and e_L (horizontal and lateral deviations from the desired landing point P) and orientation error e_θ. As the UAV descends, the marker's apparent size in the camera frame naturally increases. Our system actively reduces the physical marker size to maintain optimal detection characteristics throughout the descent.

B. Display System Considerations

While our implementation employs e-ink technology, the adaptive marker system is compatible with various display technologies. Each technology presents distinct trade-offs: LCDs offer faster refresh rates but poor sunlight visibility, OLED displays provide excellent contrast but suffer from high power consumption and UV degradation, while LED matrices excel in low-light conditions but with limited resolution. The e-ink implementation detailed in this paper prioritizes power efficiency and outdoor visibility, though applications with different priorities (e.g., night operations) may benefit from alternative display technologies or hybrid approaches.

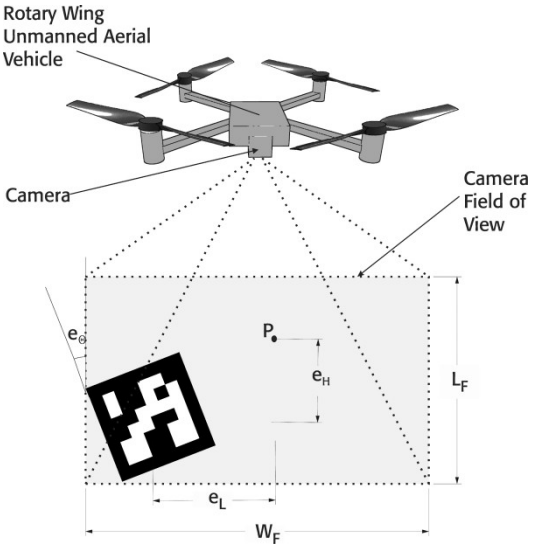

Figure 1. System overview showing coordinate frames, key dimensions, and error definitions

C. State Space Representation

The general framework combines vehicle dynamics and marker configuration in an augmented state vector:

$$x_a = [x_v, m_c]^T \in R^{17} \quad (1)$$

where x_v represents vehicle states:

$$x_v = [x, y, z, \dot{x}, \dot{y}, \dot{z}, \ddot{x}, \ddot{y}, \ddot{z}, \varphi, \theta, \psi, p, q, r] \quad (2)$$

Here, (x, y, z) denotes position in the inertial frame, (ẋ, ẏ, ż) velocities, (ẍ, ÿ, z̈) accelerations, (φ, θ, ψ) Euler angles, and (p, q, r) angular rates. The marker configuration m_c includes marker scale and pattern number.

D. Adaptive Marker System

The e-ink display enables dynamic presentation of fiducial markers from a discrete set of configurations:

$$M = \{M_1, \dots, M_N\} \quad (4)$$

Each configuration $M_i = (s_i, p_i)$ is characterized by size s_i and pattern p_i. Our implementation uses a single pattern with varying sizes determined by the height-based adaptation function:

$$s = f(z) = s_0 * \left(\frac{z}{z_0}\right) \quad (5)$$

where s_0 is the initial marker size and z_0 is the starting height. This mapping must satisfy practical constraints:

i. Visibility requirements: $h_{(M_i)} \leq z \leq h_{(M_i)}$)
ii. Display refresh time: $t - t_{last_{switch}} \geq t_r$ (1 to 3 seconds for e-ink implementation)
iii. Marker determinacy during transitions. The system must ensure that during e-ink refresh cycles, the displayed pattern cannot be misinterpreted as another valid marker in the system's lexicon. This is particularly important as e-ink displays show intermediate states during transitions that could potentially be misidentified as valid markers, leading to false position estimates.

E. Measurement Model

The measurement process combines visual marker detection with inertial sensing:

$$z = h(x_a, M_{\{m_c\}}) + v(t)) \quad (6)$$

with measurement covariance:

$$R(t) = R_b + \lambda(M_{\{m_c\}})R_m \quad (7)$$

where R_b represents baseline sensor covariance and R_m accounts for marker-dependent uncertainty.

F. Dual-Stage Estimation Framework

The system employs two coupled Kalman filters:

State Estimation Filter:

$$\hat{x}_{\{k-1\}} = f(\hat{x}_{\{k-1\}}, u_{\{k-1\}}, \hat{\theta}_{\{k-1\}}) \quad (8)$$

$$P_{\{k-1\}} = F_k P_{\{k-1\}F_k^T} + Q_k \quad (9)$$

Parameter Estimation Filter:

$$\hat{\theta}_{\{k-1\}} = \hat{\theta}_{\{k-1\}} \quad (10)$$

$$P_{\{k-1\}} = P_{\{\theta,k-1\}} + Q_{\{\theta,k\}} \quad (11)$$

G. Marker Transition Management

Display refresh latency (particularly significant in e-ink implementations) necessitates predictive transition scheduling:

$$t_{next} = t + \left(t_r, \frac{\Delta z}{\hat{v}_z}\right) \quad (12)$$

During transitions, measurement uncertainty is adjusted:

$$R(t) = \{R_b + \lambda(M_{\{m_c\}})R_m \ \ if\ |t - t_{last}| > t_r\ R_b + \kappa R_m \quad otherwise\ \} \quad (13)$$

where κ represents increased uncertainty during transitions.

IV. UNIVERSAL LANDING PROTOCOL FRAMEWORK

This section presents an overview of a protocol framework that enables reliable communication between the landing platform (hereafter referred to as the "lander") and approaching UAVs. The framework addresses two key implementation scenarios: fully integrated systems where both drone and lander are part of a unified ecosystem, and universal deployments where the landing infrastructure must accommodate unknown drones.

Between these extremes lies a spectrum of partial integration possibilities, each with different capabilities for altitude reporting and system coordination. The framework

addresses the unique challenges of adaptive marker systems, particularly the need for accurate altitude information to optimize marker characteristics while maintaining compatibility across this integration spectrum. By defining standardized interfaces and communication methods, the protocol enables implementations ranging from commercial systems with full drone-lander integration to public landing infrastructure serving unknown UAVs, while minimizing power consumption and computational overhead. The complete protocol specification is available as a separate technical document.

A. Protocol Requirements and Approaches

The fundamental challenge in precision landing is obtaining accurate altitude information while maintaining universal compatibility across different integration scenarios. Two distinct approaches emerge for this critical requirement:

i. *Passive Visual Detection (PVD)* enables completely non-integrated operation by relying solely on optical observation of approaching aircraft. This approach eliminates the need for any drone-side modifications, making it ideal for universal landing infrastructure.

ii. *Active Altitude Signalling (AAS)* represents a minimal-integration strategy that significantly enhances precision through the addition of a simple transmitter to the drone platform. Operating with a power budget of less than 100 mW, this approach bridges the gap between fully integrated and universal systems.

The protocol must accommodate both approaches while satisfying three core requirements:

i. *Reliability:* the protocol must be capable of robust altitude reporting across varying environmental conditions.

ii. *Universal Compatibility:* it should require minimal drone-side modifications; independence from specific flight control systems, and support for both known and unknown UAV platforms

iii. Resource Efficiency: power consumption should be minimal on the drone side, of the order of 50 mW.

B. Protocol Architecture

The protocol requirements of reliability, universal compatibility, and resource efficiency directly inform the architectural design. Reliability demands clear separation of concerns across protocol layers to enable robust error handling and recovery. Universal compatibility requires standardized interfaces at each layer to support both PVD and AAS approaches. Resource efficiency is achieved through optimized data flows and shared components where possible. These considerations lead to a three-layer architecture that handles both passive observation and active communication:

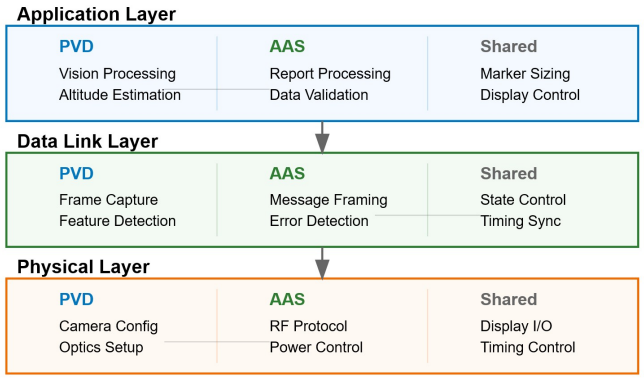

Figure 2. Universal landing protocol architecture

C. Implementation Details

The implementation of both PVD and AAS approaches requires careful consideration of hardware capabilities, timing constraints, and environmental factors.

i) PVD Implementation

PVD operates through standardized computer vision interfaces that enable altitude estimation without drone-side modifications. The protocol defines three processing stages: frame acquisition, feature analysis, and altitude computation. The frame acquisition stage specifies requirements for camera timing and synchronization. Feature analysis establishes methods for UAV detection and tracking across the field of view, while the altitude computation stage defines how dimensional constraints should be applied for consistent height estimation.

ii) AAS Implementation

AAS provides a lightweight communication solution when limited access to UAV systems is available. This approach allows integration of a low-power transmitter into the UAV, enabling direct altitude reporting without compromising battery life or requiring complex hardware modifications. The protocol defines a 24-bit message structure with fields for synchronization, altitude data, status flags, error detection, and future extensions.

V. IMPLEMENTATION AND EXPERIMENTAL VALIDATION

A. Hardware Setup

The experimental platform (Figure 3) implements a modified F450 quadrotor equipped with a custom landing interface. At its core, the system utilizes a Pixhawk 4 flight control unit (FCU) based on the STM32F765 ARM Cortex-M7 processor operating at 216 MHz. The FCU integrates key navigational sensors including a temperature-stabilized ICM-20689 IMU, BMM150 3-axis magnetometer, and MS5611 barometric pressure sensor. System control is managed through a customized implementation of PX4 firmware (v1.13.2), specifically optimized for high-precision autonomous landing operations. Visual sensing is achieved through a nadir-mounted Firefly Hawkeye camera system, incorporating a wide-angle CMOS sensor with 170° field of view. The camera supports multiple resolution modes ranging from 4K

(3840×2160@24fps) to high-speed 720p (1280×720@120fps), with dynamic exposure and gain control mechanisms implemented to optimize fiducial marker detection and tracking.

For AAS implementation, several RF transceivers were evaluated against the protocol requirements: 24-bit message structure (8-sync, 8-alt, 2-status, 2-error, 4-reserved bits), reliable error detection/recovery, 20m operational range, real-time altitude reporting, and consistent operation during marker transitions. The evaluated options included the Texas Instruments CC1101, Nordic Semiconductor nRF24L01+, Silicon Labs Si4063/64, and Hope RF RFM69. The nRF24L01+ was selected for its optimal combination of power efficiency (37.3mW at 0dBm, 23.1mW at -12dBm), 2Mbps maximum data rate, built-in auto-retransmission, and comprehensive error handling features. The transceiver operates at 2.4GHz and interfaces with the Pixhawk through SPI, with custom firmware handling protocol timing and power management.

The landing platform utilizes a 13.3-inch e-ink display (1600×1200 resolution) driven by an IT8951 controller through SPI/USB interface. The display provides 170° viewing angle and 16-level grayscale capability, achieving 1-second full refresh rates through optimized waveform look-up tables and partial refresh modes. Visual detection is implemented using a 16 Megapixel Firefly Q6 Hawkeye camera (4608×3456) with a 1/2.3-inch CMOS sensor, providing 170° field of view and wide dynamic range capability. The AAS receiver implements a second nRF24L01+ module configured in receive mode, with dual-antenna diversity achieving -104dBm sensitivity at 250kbps.

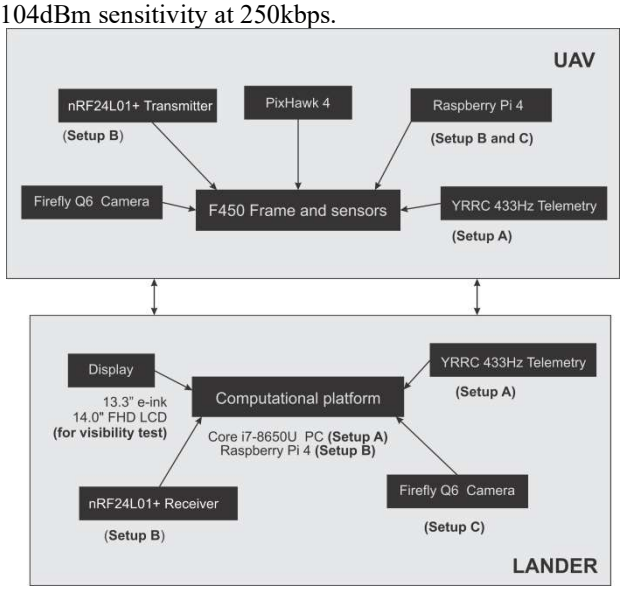

Figure 3. System hardware architecture showing key components and interfaces

System control and protocol implementation are managed by a Lenovo Carbon X1 laptop with an Intel Core i7-8650U processor at 1.90 GHz and 16 GB of DDR4 memory. Connecting Raspberry Pi Compute Module 4 (8GB variant) allowed direct interfaces for display control (SPI), RF communication (SPI), and camera input (MIPI CSI-2), with precise timing maintained through a dedicated real-time clock, as detailed in Figure 3. [used telemetry between drone and PC, used to test a full integrated approach where operator has access to all aspects of lander and drone. AAS transceivers used to test semi-integrated.

B. Software Implementation

i) ArUco Detection Pipeline

The vision system implements a real-time detection pipeline optimized for precision landing operations, processing frames at 30Hz using the FireFly Q6 Hawkeye. As shown in Figure 4, the pipeline comprises three primary stages: frame acquisition, marker detection, and pose estimation. The figure shows how a single acquire frame is processed.

The frame acquisition stage downsamples the native 1920×1080 resolution to 640×480 for processing efficiency. A grayscale conversion precedes the detection phase to enhance robustness. Marker detection employs the ArUco 4×4 dictionary (DICT_4X4_100) with ID 23 designated for landing operations. Detection parameters are optimized through adaptive thresholding with marker-scaled windows, sub-pixel corner refinement, and temporal false-positive rejection.

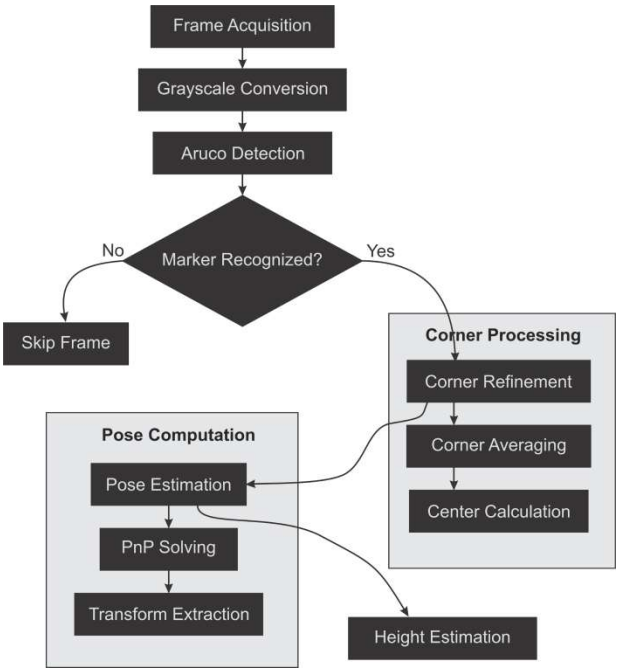

Figure 4. Frame processing pipeline

ii) Kalman Filter Implementation

The dual-stage estimation framework, depicted in Figure 5, combines state and parameter estimation through parallel Kalman filters. The state estimator tracks an 8-dimensional vector:

$$x_s = [x, \dot{x}, \ddot{x}, y, \dot{y}, \ddot{y}, z, \dot{z}]^T \quad (14)$$

implementing a constant acceleration model with Δt = 0.33s through the state transition equations:

$$[Position_k + 1] = [1 \ \Delta t \ \tfrac{1}{2}\Delta t^2][Position_k] \quad (15)$$

$$[Velocity_k + 1] = [0 \ 1 \ \Delta t][Velocity_k] \quad (16)$$

$$[Acceleration_k + 1] = [0 \ 0 \ 1][Acceleration_k] \quad (17)$$

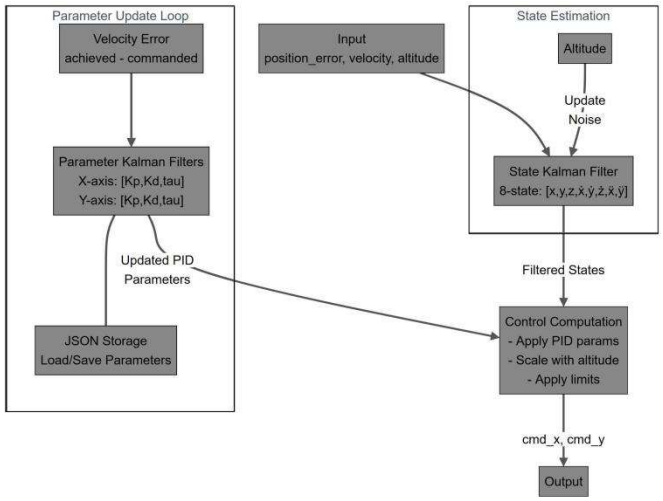

Figure 5. Dual-stage Kalman filter architecture showing parallel state and parameter estimation paths

Process noise adaptation follows height-dependent interpolation:

$$Q(h) = diag([q_{x(h)}, q_{x(h)}, q_{x(h)}, q_{y(h)}, q_{y(h)}, q_{y(h)}, q_{z(h)}, q_{z(h)}]) \quad (18)$$

where $q_{x(h)}$ and $q_{y(h)}$ are derived from empirical measurements at 5m and 15m altitudes.

Parameter estimation maintains independent 4-dimensional state vectors:

$$\theta = [Kp, Ki, Kd, \tau]^{\mathrm{T}} \quad (19)$$

for each axis, with τ representing system delay. The measurement model compares achieved versus commanded UAV velocities:

$$z = v_{actual} - v_{cmd} \quad (20)$$

using conservative process noise:

$$Q_{param} = diag([0.001, 0.001, 0.001, 0.0001]) \quad (21)$$

Cross-coupling occurs through command generation:

$$v_{cmd} = -Kp(x_{est}) - Kd(\dot{x}_{est}) \quad (22)$$

$$v_{compensated} = \frac{vcmd}{Kp_{est}} + \dot{x}_{est}\left(\frac{\tau_{est}}{Kp_{est}}\right) \quad (23)$$

Parameter persistence across sessions uses JSON serialization, initializing with Kp = 0.5, Ki = 0.0, Kd = 0.02, and τ = 0.28.

iii) Display Control System

The e-ink display control system manages marker presentation through a predictive scheduling framework. The system compensates for the inherent 1-second refresh latency through descent rate estimation and proactive uncertainty management. Figure 6 illustrates the timing relationships between altitude reports, marker transitions, and state updates, showing how continuous tracking is maintained through display refresh cycles. The controller implements a non-uniform quantization scheme across the 20-meter operating range, providing 1cm resolution at 0-1m, 2 cm resolution at 1-3 m, 10 cm resolution at 3-10m, and 20 cm resolution at 10-20 m heights.

C. Test Methodology

The experimental validation consisted of four sequential tests designed to characterize system performance. First, we evaluated marker detection reliability under varying lighting conditions by comparing the 13.3-inch e-ink display with a 14-inch LCD display (170° viewing angle, 700:1 contrast ratio, 297 nits brightness). Both displays showed an ArUco 4×4 marker (ID: 23) with physical dimensions of 16.7 cm per side. The test UAV was flown over each display under illuminance conditions ranging from 1 to 100,000 lux, measured using a TES 1330C light meter.

To evaluate the impact of e-ink refresh time on landing performance, we positioned the UAV at 3 meters elevation and executed two distinct marker size transitions. Tests were conducted under 79,000 lux ambient illumination to ensure optimal e-ink visibility. Video was captured at 30 frames per second, with subsequent manual processing to determine the proportion of frames containing valid marker detections during the transition period.

Landing precision tests compared adaptive versus static marker approaches through 20 landing trials from a 3-meter initial height. For the adaptive marker tests (n=10), the e-ink display progressively reduced the marker size from 16.7 cm to a final dimension of 2.8 cm × 2.8 cm just before landing. The remaining trials (n=10) maintained a fixed 16.7 cm marker size. Landing accuracy was measured by marking reference points on the landing surface and using a vernier caliper to measure the displacement between the UAV's final position and the intended landing point.

Finally, we investigated the dual-stage Kalman filter's impact on system performance by comparing position error profiles with and without learned PID parameters. The parameters were preserved between sessions in a JSON file, which could be deleted to reset the learning process. We recorded the variation in positioning error during descent, comparing the initial performance (no learned parameters) with that achieved after four landing iterations. This enabled quantification of the filter's learning effectiveness and its contribution to landing precision using the root-mean-square error (RMSE) metric. All tests were conducted under consistent environmental conditions with wind speeds below 15 km/h.

For the size-transition analysis presented in Figure 6, still frames were extracted at regular intervals during descent. Frame capture occurred every 50 cm of descent from 14 m down to 2 m altitude, then at closer intervals of every 10 cm from 2 m to touchdown to capture the critical final approach phase. The adaptive marker scaling system was triggered when the barometric and vision-fused altitude estimate fell below 10 m, following the relationship

$$s(h) = max(2.8\ \text{cm}, 16.7\ \text{cm} \cdot h/10) \quad \text{for } h \leq 10\text{m} \quad (24)$$

This scaling function used the 16.7 cm dimension as the largest displayable square marker, with the 10 m threshold

representing the altitude where control transitioned from barometric to vision-based systems. The lower bound of 2.8 cm was established based on the vision system's minimum reliable pixel footprint for consistent marker detection.

VI. RESULTS AND DISCUSSION

The marker detection performance exhibited strong illumination dependence across display technologies (Table 1). The e-ink display demonstrated optimal performance under high ambient light conditions, achieving reliable detection up to 14.2m under direct sunlight (100,000 lux), while becoming undetectable below 10 lux due to its reflective operating principle. This behavior aligns with the fundamental physics of e-ink displays, where image formation relies on ambient light reflection from suspended particles rather than active illumination. The detection range shows a nearly linear relationship with ambient illumination above 100 lux, suggesting that the limiting factor is the camera's ability to capture sufficient contrast rather than the display's inherent characteristics.

Conversely, the LCD display showed inverse performance characteristics, with peak detection range of 13.8m under overcast conditions (1,000 lux), suggesting an optimal contrast ratio between display luminance and ambient illumination. This peak performance at moderate illumination levels can be attributed to the competition between display backlight intensity and ambient reflection from the LCD surface. At high illumination levels, surface reflections overwhelm the display's output, while in low-light conditions, the display's maximum brightness of 297 nits proves sufficient for reliable detection up to 7.6m.

Table 1. Maximum marker detection heights under varying ambient illumination conditions for e-ink and LCD displays

SN	Illuminance (lux)	Ambient Condition	Maximum height (m)	
			e-ink	LCD
1	100,000	Sunlight	14.2	0
2	10,000	Full Daylight	13.0	11.2
3	1,000	Overcast Day	12.0	13.8
4	100	Very Dark Day	6.8	12.2
5	10	Twilight	0	8.4
6	1	Night	0	7.6

This complementary behavior suggests potential for hybrid systems in applications requiring 24-hour operation, though power consumption and system complexity trade-offs would need careful consideration. Such a hybrid system could theoretically achieve consistent detection ranges above 13m across all lighting conditions by automatically selecting the optimal display technology based on ambient illumination levels. However, the added complexity of dual display systems, synchronization requirements during transitions, and increased power consumption (particularly from the LCD backlight) would need to be weighed against operational requirements. The data also suggests that for dedicated daylight operations, the e-ink display's combination of high visibility and minimal power consumption makes it the clearly superior choice.

The e-ink refresh sequence analysis (Figure 6) revealed a transition pattern that balances update speed with detection reliability. The sequence, captured at 30 frames per second, spans 36 total frames (1.2 seconds), though Figure 6 shows every third frame for clarity, resulting in 100ms intervals between displayed frames. Traditional e-ink displays employ a sequential process: first, a global voltage reset converts all cells to white, followed by selective voltage application to achieve desired grayscale states. However, our implementation utilizes newer partial refresh technology, which attempts to transition directly to the new state without an initial global reset. This optimization becomes evident in Frame 5, where the marker begins its size reduction to 90% of its original dimensions, attempting to minimize detection interruption.

The first manifestation of the new marker size appears in Frame 5, with a clean version emerging by Frame 7, though this is temporarily interrupted by the traditional white-flash reset phase spanning Frames 9-10. Critical for real-time tracking, valid marker detection resumes from Frame 7, limiting the maximum detection interruption to 500ms (equivalent to 15 frames at 30 fps). This temporal characteristic, while significantly longer than LCD refresh rates, proved manageable through the dual-stage Kalman filter's predictive capabilities.

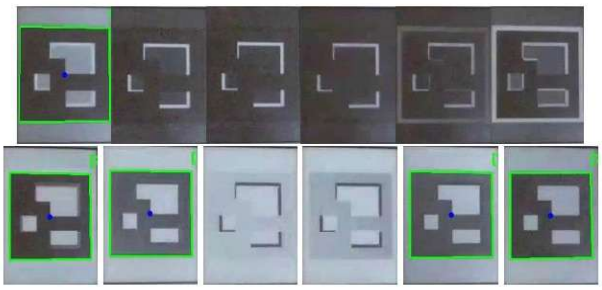

Figure 6. Sequence of frames during a refresh of the e-ink display. Note that this sequence shows only every third frame from a fuller sequence acquired at 30 frames per second.

The results of the landing precision test are shown in Table 2. The improvement in landing precision is evident from the table. The mean displacement between desired final landing position and actual landing position when using the adaptive marker is 1.95 cm while using the adaptive marker. This compares with a mean displacement of 4.80 cm while using the fixed marker. The performance of the adaptive marker-based system is justifiable given the fact that the marker shrinks all the way down to 2.8 cm just before landing. In fact, achieving even better results was limited only by the horizontal stability of the UAV as it got closer to the landing surface. From a purely vision-based perspective, centralizing the camera over

a 2.8 cm marker could result in much lower error than 1.95 cm. as noted however, at the last moment of landing, the UAV is not perfectly stable; the legs do not all hit the landing surface at the same time, which limits the accuracy that might otherwise have been achieved.

Table 2 Results from 10 landings each using adaptive and fixed marker sizes

Landing Number	**Adaptive Marker Error (cm)**	**Fixed Marker Error (cm)**
1	1.9	4.8
2	1.7	4.4
3	2	5
4	2.4	5.6
5	1.7	4.3
6	2.4	4.3
7	2.1	5.6
8	1.6	5
9	2	4.1
10	1.7	4.9
Mean	1.95 ±0.29	4.80±0.53

To quantify the effect of wind on landing accuracy, additional landing trials were conducted under varying natural wind conditions. The windspeed was measured with a handheld anemometer. The results, summarized in Table 3 below, show that mean lateral landing error gradually increases as wind speed increases up to 15 km/h. This confirms that while the system remains robust under moderate wind, wind is a significant factor affecting precision.

Table 3 Effect of wind speed on mean lateral landing error

Wind speed (km h^{-1})	**Mean lateral error (cm)**	**σ (cm)**
0	1.95	0.29
5	2.47	0.31
10	3.02	0.38
15	3.60	0.41

Beyond wind, two secondary factors were found to correlate with error growth. First, low ambient illuminance below 30 lx reduces the e-ink display's contrast, which occasionally produces false rejections during marker detection; this effect was quantified by monitoring ambient illuminance across a range of 1 to 100,000 lx. Second, ground-effect turbulence during the final descent causes momentary frame blur that can lead to small pose estimation deviations; vibration spectra in the 0–50 Hz band were recorded from the Pixhawk IMU to characterize this phenomenon.

The performance of the Kalman filter was estimated using the root-mean-square error in pixels recorded on each axis during a landing initiated from an altitude of 3 m. Every frame processed by the OpenCV library throughout the landing was saved, and the error (in pixels) between the desired and actual location of the UAV over the marker was recorded. Repeated for 4 sequential landings, this resulted in Table 4. The gradual improvement from landing to landing suggests that the Kalman filter is learning the parameters of the UAV's internal PID velocity control.

Table 4. RMSE values (in pixels) showing Kalman filter positioning improvement over sequential landings

	Landing 1		**Landing 2**		**Landing 3**		**Landing 4**	
	X	**Y**	**X**	**Y**	**X**	**Y**	**X**	**Y**
RMSE(pixels)	15 0.3	17 0.8	15 4.1	16 8.3	14 3.2	162 .77	14 0.5	15 1.4

The comparative analysis of our adaptive marker system against existing precision landing approaches reveals substantial advancements in landing accuracy and reliability. Our achieved mean landing error of 1.95cm represents a significant improvement in precision landing capability. This performance substantially exceeds previous approaches: passive reflector systems (Yasentsev et al., 2021) achieving 1-3m accuracy, photodiode-based localization (Bastiaens et al., 2021) reaching 3.5cm accuracy, simplified AprilTag implementations (Wang et al., 2017) attaining 10 cm accuracy, and vision-inertial approaches using traditional Kalman filtering (Yuan et al., 2017) achieving 6 cm accuracy. The marked improvement can be attributed to three key innovations: the dynamic marker adaptation strategy that maintains optimal detection characteristics throughout descent; the dual-stage Kalman filter architecture that simultaneously handles state estimation and parameter adaptation while managing display transition dynamics; and the universal protocol framework enabling robust operation across varying integration scenarios.

VII. CONCLUSION

This paper has presented a novel approach to precision UAV landing through adaptive-size fiducial markers and dual-stage Kalman filtering. The system achieves mean landing errors of 1.95 cm under wind conditions up to 15 km/h, representing a 59% improvement over fixed-marker approaches. The Universal Landing Protocol framework extends precision landing capabilities to both integrated and unknown UAV systems through its dual-mode approach, combining Passive Visual Detection and Active Altitude Signalling with minimal resource overhead. While the e-ink implementation proves the concept's viability, limitations include the 1-second refresh latency constraining descent rates. Future work may explore hybrid display technologies for 24-hour operation, enhanced marker patterns, and integration with emerging UAV standards, leveraging the framework's extensibility through reserved protocol bits.

AUTHOR CONTRIBUTIONS

K. P. Ayodele: Conceptualization, Methodology, Validation, Writing – original draft, Writing – review & editing. **P. T. Okewunmi:** Software development, Experimentation, Data analysis, Writing – review & editing. **S.**

O. Akinola: Setting up the flight experiment, Data analysis Validation. **A. A. Ogunseye:** Supervision, Writing – review & editing. **M. I. Eghrudje:** Implementation of Kalman filter, Writing – original draft. **F.B. Offiong:** Supervision, Funding acquisition. **S. P. Olayiwola:** Software development, Experimentation, Data analysis. **A. R. Lawal:** Writing-Proofreading of the manuscript, Implementation of signal processing firmware. **F. O. Akinluyi:** Supervision, Funding acquisition. **A. A. Ishola:** UAV flight planning, Writing-review and editing.

ACKNOWLEDGEMENT

The researchers wish to thank the Tertiary Education Trust Fund (TETFUND) for supporting this work under the National Research Fund (NRF) programme.

REFERENCES

Arents, R., Groeneweg, J., Mulder, M., & Van Paassen, M. (2009). Predictive landing guidance in synthetic vision displays. *In AIAA Guidance, Navigation, and Control Conference* (p. 5984). https://doi.org/10.2514/6.2009-5984

Bastiaens, S., Mommerency, J., Deprez, K., Joseph, W., & Plets, D. (2021). Received signal strength visible light positioning-based precision drone landing system. *In 2021 International Conference on Indoor Positioning and Indoor Navigation (IPIN)* (pp. 1–8). IEEE. https://doi.org/10.1109/IPIN51102.2021.9634055

Borowczyk, A., Nguyen, D. T., Phu-Van Nguyen, A., Nguyen, D. Q., Saussié, D., & Le Ny, J. (2017). Autonomous landing of a multirotor micro air vehicle on a high velocity ground vehicle. *IFAC-Papers OnLine*, 50(1), 10488–10494. https://doi.org/10.1016/j.ifacol.2017.08.2032

Cabrera-Ponce, A. A., & Martinez-Carranza, J. (2017, October). A vision-based approach for autonomous landing. *In 2017 Workshop on Research, Education and Development of Unmanned Aerial Systems (RED-UAS)* (pp. 126–131). IEEE. https://doi.org/10.1109/RED-UAS.2017.8116073.

Claro, R. M., Silva, D. B., & Pinto, A. M. (2023). ArTuga: A novel multimodal fiducial marker for aerial robotics. *Robotics and Autonomous Systems*, 163, 104398. https://doi.org/10.1016/j.robot.2023.104398

Ferrão, J. M. L. (2023). A multimodal vision-based sensor fusion approach for precise landing of an UAV (Master's thesis). Universidade do Porto, Portugal.

Nguyen, P. H., Kim, K. W., Lee, Y. W., & Park, K. R. (2017). Remote marker-based tracking for UAV landing using visible-light camera sensor. *Sensors,* 17(9), 1987. https://doi.org/10.3390/s17091987

Park, Y., Song, W., Lee, C., Kwon, J., & Park, J. (2024). Fiducial marker-based autonomous landing using image filter and Kalman filter. *International Journal of Aeronautical and Space Sciences,* 25(1), 190–199. https://doi.org/10.1007/s42405-023-00605-2

Pieczyński, D., Ptak, B., Kraft, M., Piechocki, M., & Aszkowski, P. (2024). A fast, lightweight deep learning vision pipeline for autonomous UAV landing support with added robustness. *Engineering Applications of Artificial Intelligence*, 131, 107864. https://doi.org/10.1016/j.engappai.2023.107864

Ulrich, J., Alsayed, A., Arvin, F., & Krajník, T. (2022). Towards fast fiducial marker with full 6 DoF pose estimation. In *Proceedings of the 37th ACM/SIGAPP Symposium on Applied Computing* (pp. 723–730). https://doi.org/10.1145/3477314.3507636

Wang, Z., She, H., & Si, W. (2017). Autonomous landing of multi-rotors UAV with monocular gimbaled camera on moving vehicle. In *2017 13th IEEE International Conference on Control & Automation (ICCA)* (pp. 408–412). IEEE. https://doi.org/10.1109/ICCA.2017.8284507

Wu, Y., Niu, X., Du, J., Chang, L., Tang, H., & Zhang, H. (2019). Artificial marker and MEMS IMU-based pose estimation method to meet multirotor UAV landing requirements. *Sensors*, 19(24), 5428. https://doi.org/10.3390/s19245428

Wubben, J., Fabra, F., Calafate, C. T., Krzeszowski, T., Marquez-Barja, J. M., Cano, J. C., & Manzoni, P. (2019). Accurate landing of unmanned aerial vehicles using ground pattern recognition. *Electronics,* 8(12), 1532. https://doi.org/10.3390/electronics8121532

Yasentsev, D., Shevgunov, T., Efimov, E., & Tatarskiy, B. (2021). Using ground-based passive reflectors for improving UAV landing. *Drones*, 5(4), 137. https://doi.org/10.3390/drones5040137